International Journal of Impact Engineering 57 (2013) 55–69

Contents lists available at SciVerse ScienceDirect

International Journal of Impact Engineering

journal homepage: www.elsevier.com/locate/ijimpeng

Shock analysis and optimization of two-layered cellular materials subject to pulse loading

John C. Goetz, Karel Matouš*

Department of Aerospace and Mechanical Engineering, University of Notre Dame, Notre Dame, IN 46556, USA

ARTICLE INFO

Article history:
Received 7 September 2012
Received in revised form
22 November 2012
Accepted 4 January 2013
Available online 8 February 2013

Keywords:
Shock wave
Plasticity
Optimization
Cellular material

ABSTRACT

We present the method of characteristics with mass, momentum, and energy conservation to solve the nonlinear wave equation with shock formation in a two layer one-dimensional rod made of cellular material. We show that the rigid-perfectly-plastic-locking model cannot predict shock formation at a material interface, so we propose an elastic–plastic-densifying model to describe the stress–strain behavior of the cellular materials. The conditions for shock formation at a material interface are provided. We conduct a two-layer analysis to gain insights into the behavior of two layer cellular systems and to determine which material properties are most important for design. Finally, we optimize the significant parameters to reduce the length of one and two layered cellular systems with impulse and mass constraints subject to pulse loading. The results reinforce the concept of sandwich structures and show that two layer systems can achieve a 30% reduction in length over single layer ones.

1. Introduction

Cellular materials (e.g., foam, honeycomb, lattice structures) have proven indispensable in a variety of applications such as insulation, filler for light-weight structural elements, packaging, and, more recently, armor. It is the ability to absorb significant input energy while transmitting relatively little load that makes cellular materials appealing for protective applications [1]. The protective capability of these materials is a function of their stress–strain behavior and their highly heterogeneous nature [2]. Experimental evidence confirms that shock fronts can form within cellular materials subject to dynamic impact loading [3–8]. Under the right conditions, shock formation can increase the energy absorbing capacity of cellular materials without increasing the transmitted load.

A number of analytical and numerical methods can be used to analyze the behavior of a cellular material under a dynamic event. The detailed numerical methods model the entire cellular structure (e.g. lattices [9] or voronoi foam [10]) in two or three dimensions and solve the dynamic problem with the finite element method (FEM), for example. To reduce the complexity of the analysis, the cellular material is sometimes represented as a homogeneous medium in the FEM analysis, when the scale of the element is sufficiently large to encompass the unit cell of the material [11–13]. Reducing the problem to a single dimension is done to develop analytical solutions that provide insights into the behavior of cellular systems under pulse loadings, such as the minimum impact speed to induce shock formation [10].

A number of methods have been proposed to solve the one-dimensional shock problem in cellular materials, including spring-mass models [14,15], energy balance [16–19], purely mechanical mass and momentum conservation [13,20,21], and the method of characteristics in conjunction with a complete thermo-mechanical conservation analysis [10,22,23]. Note that some of the models, i.e., spring-mass and energy balance, are regarded today as less accurate and potentially flawed. Nevertheless, their introduction allowed future research to be performed in the right direction of thermodynamically consistent mass, momentum and energy conservation. The majority of these works use a rigid-perfectly-plastic-locking (RPPL) model to describe the stress–strain relationship of the cellular material. Only a few works have included elasticity [14,15,20]. In [20], elasticity is only applied to regions of material that are not fully compacted. Once the material has fully collapsed it is treated by the RPPL model. Omitting elasticity in favor of the RPPL model simplifies the problem enough for a closed form solution to be obtained [10]. A closed form solution is advantageous for optimization studies and allows for the optimal (e.g., minimum) length necessary to defeat a specified load to be calculated [20]. However, most of these works limit analysis to a single material layer of foam.

The method of characteristics is frequently applied to single material problems of elastic nature [23–25], as well as elasto-plastic problems [25–27], and in conjunction with mass,

* Corresponding author.
E-mail address: kmatous@nd.edu (K. Matouš).

0734-743X/$ – see front matter © 2013 Elsevier Ltd. All rights reserved.
http://dx.doi.org/10.1016/j.ijimpeng.2013.01.001

momentum, and energy conservation to treat the wave problem when shocks are involved [8,22,23]. The NASA report by Utku [23] uses the method of characteristics to calculate shock wave formation at the impact surface of two elasto-plastic bodies, but does not examine the behavior of two materials working together in series to dissipate an applied load. A thorough analysis of the behavior of multi-layered systems subject to pulse loading, particularly analysis of the system response to variations in the properties of the material layers and their optimization, is still lacking.

In the area of armor design, it is acknowledged that better armor performance can be achieved through the layering of different materials [1]. A few works discuss multi-layered cellular systems [21,26,28,29]. Sumi [26] does not explicitly explore the problem, but mentions that finite difference method and the method of characteristics can be used to solve it. Ma and Ye [21] use a stress based analysis on a two layer system with a rigid mass between the layers with the RPPL model to describe the material behavior. However [21], does not address shock formation in two-layer systems. Maheo and Viot [28] and Zeng et al. [29] perform experimental and FEM numerical analysis on the macroscopic behavior of multi-layered foams under quasi-static and dynamic loads. While providing useful insights into the behavior of layered materials, Maheo and Viot [28] perform no optimization and do not address shock formation. Konstantinov et al. [30] investigates a two layer problem where the first layer is elasto-plastic and the second layer is an infinite elastic bar. The method of characteristics is used in [30] with a bilinear material model. Although strong discontinuities are discussed, shocks are not examined and since the second layer is infinitely long, complex wave interactions are avoided.

Optimization of the material parameters as a way of improving the performance of the system has been investigated in [12,31–34]. Several works focus on the design of microstructure [31–33]. Optimization of macroscopic parameters has also received attention [12,34]. For example, Zhu et al. [34] examines the effects of changing length and density on the maximum deflection of a foam sandwich plate using energy balance and Cui et al. [12] optimizes acceleration of a fixed volume foam panel that is functionally graded using finite element analysis. Shen et al. [35] provides insights into the behavior of functionally graded cellular materials and derive analytical expressions for shock formation using the RPPL model. In Shen's work, the only free parameter is the yield stress gradient. The gradient is varied from positive to negative slope to study its influence on shock formation and energy absorption. Unfortunately, shock formation and its influence on the optimality of a cellular system are rarely discussed.

This work uses the method of characteristics to solve the nonlinear wave equation with mass, momentum, and energy conservation to treat shock formation in a two layer one-dimensional rod made of cellular material. A number of features set this work apart from previous efforts. We will show that the RPPL model is incapable of predicting shock formation at the material interface, and so a fully elastic–plastic-densifying model is used throughout the analysis. Next, a two layer analysis provides useful insights into the behavior of two layer cellular systems. A sensitivity study is conducted to determine which material parameters are most important for the design of a layered cellular material system. The most influential parameters are then optimized to improve the performance of one and two layered cellular systems subject to pulse loading.

A description of the material model is covered in the first section of this paper (Section 2.1), followed by the description of the characteristics and thermodynamic shock theory in Section 2.2. Shock formation at the interface is covered in Section 2.3 followed by a description of the numerical implementation of the method of characteristics in Section 2.4. Section 3 covers the verification of the current work and the two layer analysis. Optimization is covered in section 4. Finally, some conclusions are drawn in Section 5.

2. Shock analysis of two-layer systems

This work will consider two different layers of cellular material as shown in Fig. 1. Here $X \in \mathbb{R}^1$ designates the position of material points in the reference configuration $\Omega_0 \in \mathbb{R}^1$ in the Cartesian coordinate system and $x(X,t)$ is the spatial coordinate of a particle. Note that O is the origin of the coordinate system (see Fig. 1). A pulse, of either constant stress or velocity, is applied to the left end of layer A. A number of assumptions will be made to simplify the analysis: i) shock process is adiabatic, ii) stress is a function of strain only, iii) input loads are piecewise constant, iv) a cellular material is represented as a homogeneous medium in bulk, and v) the material does not fracture.

2.1. Constitutive law

The stress–strain behavior of cellular materials under compression is typically characterized by a short elastic region, followed by a relatively flat "plateau" region, followed by a densification region (see Fig. 2). A number of previous works [10,13,20,22,36,37] have utilized the RPPL model for cellular materials as a close approximation. It will be shown that elastic waves become important in the two-layer problem, and so the RPPL model is abandoned in favor of a non-linear one. We shall call this model Elastic–Plastic-Densifying and abbreviate it EPD (see Fig. 2). Thus material behavior is defined by six material constants: elastic modulus E, plastic modulus H_1, densification modulus H_2, yield stress σ_y, densification strain $\bar{\varepsilon}_D$, and the reference mass density $\rho_0 = \rho_0(X,t)$. From these constants four additional parameters relevant to the analysis can be derived:

$$E_p = \frac{EH_1}{E+H_1}, \tag{1}$$

$$E_D = \frac{EH_2}{E+H_2}, \tag{2}$$

$$\sigma_D = \sigma_y + H_1\bar{\varepsilon}_D = \sigma_y + E_p(\varepsilon_D - \varepsilon_y), \tag{3}$$

$$\varepsilon_D = \frac{H_1}{E_p}\bar{\varepsilon}_D + \varepsilon_y. \tag{4}$$

Here, E_p and E_D are the elastoplastic and densification tangent moduli respectively, σ_D is the densification stress, and ε_D is the total strain at onset of densification.

We assume an additive split between elastic, and inelastic (total plastic and densification) strains as

$$\varepsilon = \varepsilon_e + \varepsilon_i. \tag{5}$$

The elastic stress–strain relationship is used

$$\sigma = E(\varepsilon - \varepsilon_i). \tag{6}$$

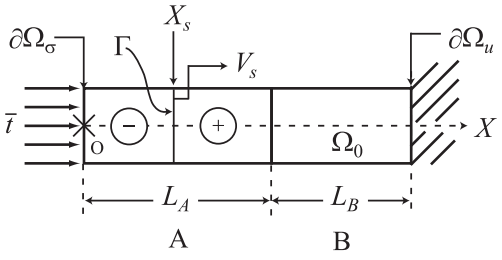

Fig. 1. Two-layered cellular material system. Note that the open domain representing the rod is $\Omega_0 = \Omega_0^{\pm} \cup \Gamma$.

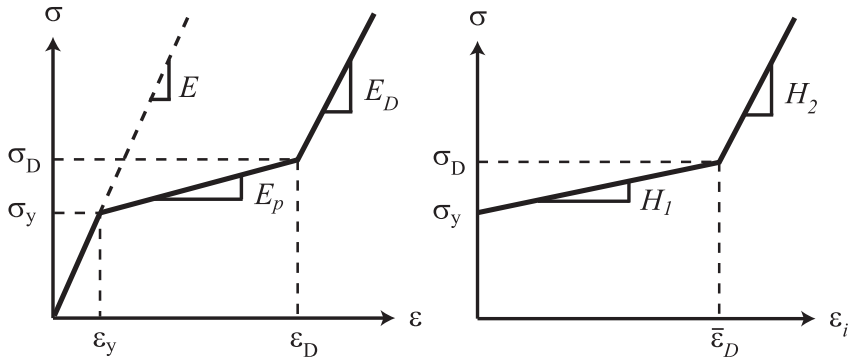

(a) EPD stress-strain law. (b) Plastic hardening/densification law.

Fig. 2. Schematic of elastic–plastic-densifying material law and material constants.

The strain hardening in the material will be modeled as isotropic using associative plasticity. The yield criterion, flow rule, hardening law, and Kuhn-Tucker loading/unloading conditions are

$$f(\sigma, \vec{\alpha}) = |\sigma| - (\sigma_y + \vec{H} \cdot \vec{\alpha}), \tag{7}$$

$$\varepsilon_i = \dot{\gamma} \frac{\partial f(\sigma, \vec{\alpha})}{\partial \sigma}, \tag{8}$$

$$\vec{\alpha} = \dot{\gamma} \frac{\partial f(\sigma, \vec{\alpha})}{\partial \vec{\alpha}}, \tag{9}$$

$$\dot{\gamma} \geq 0, \quad f(\sigma, \vec{\alpha}) \leq 0, \quad \dot{\gamma} f(\sigma, \vec{\alpha}) = 0, \tag{10}$$

where $\dot{\gamma}$ is the plastic multiplier. $\vec{H} = [H_1, H_2]$ and $\vec{\alpha} \geq \vec{0}$ is the amount of plastic deformation along each branch of $\vec{H}$. Note that for our tri-linear model E_D cannot be greater than E. The classical uniqueness condition, $1/2\dot{\sigma}\dot{\varepsilon} \geq 0$, requires that $H_1 \geq 0$ and $H_2 \geq 0$, which implies that $E_p \geq 0$ and $E_D \geq 0$ (see [38] for more details). Moreover, if $H_2 = \infty$ then $E_D = E$, which implies that $\alpha_2 = 0 \forall \varepsilon$.

It is commonly acknowledged that the material properties of a cellular material can be written as a function of relative density [39–41],

$$\rho_0 = \overline{\rho}_0 \rho_0^s, \tag{11}$$

where $\overline{\rho}_0$ is the reference relative mass density and ρ_0^s is the reference mass density of the base material (e.g., aluminum). This work will use Rohacell WF foam, whose base material is Polymethacrylimide (PMI). To describe the behavior of Rohacell WF foam, the data parametrization of Hanssen [41] is used:

$$\sigma_y = \sigma_y^s \overline{\rho}_0^n, \tag{12}$$

$$E = E^s \overline{\rho}_0^p, \tag{13}$$

$$\varepsilon_D = 1 - \overline{\rho}_0^m. \tag{14}$$

Here σ_y^s is the yield stress of the base material, n, p and m are exponents chosen to fit the available data with a power law relation. The exponent values for this work were selected to best fit the material data for Rohacell WF-51 foam that is provided by [42] in order to compare the results against the work of [20]. The values are $n = 1.5$, $p = 1.737$, and $m = 0.3712$. Although Hanssen does not include the exponent m in his model [41], it is introduced here to match the value of ε_D reported in [14].

Since this work primarily concerns two-layer systems, properties of a given layer will be referred to with a superscript A or B, i.e., the yield stress for layer A would be written as σ_y^A or the densification strain of layer B would be written as $\overline{\varepsilon}_D^B$.

2.2. Governing equations

For the completeness of the analysis, in this section we review the basic governing equations. The solution to the present problem is derived from the one-dimensional nonlinear wave equation,

$$\frac{\partial^2 u}{\partial t^2} = C(\varepsilon(u))^2 \frac{\partial^2 u}{\partial X^2} \quad \in \quad \Omega_0^{\pm}, \tag{15}$$

with

$$C = \sqrt{\frac{1}{\rho_0} \frac{\mathrm{d}\sigma}{\mathrm{d}\varepsilon}}, \tag{16}$$

where $u(X,t) = x(X,t) - X$ is the particle displacement field. To solve the wave equation, it is necessary to define initial conditions, $u(X,0) = u_0 \in \Omega_0$ and $v(X,0) = v_0 \in \Omega_0$, as well as boundary conditions, $\sigma \cdot \widehat{n} = \overline{t} \in \partial\Omega_\sigma$ and $u = \overline{u} \in \partial\Omega_u$ (see Fig. 1), where $\widehat{n}$ is the unit normal to the boundary. u_0 is the displacement field at $t = 0$, $v = \partial u/\partial t$ is the particle velocity, v_0 is the velocity field at $t = 0$, $\overline{t}$ is the prescribed stress on the boundary $\partial\Omega_\sigma$, and $\overline{u}$ is the prescribed displacement on the boundary $\partial\Omega_u$. Note that $\partial\Omega_\sigma$ and $\partial\Omega_u$ are smooth open disjoint subsets of $\partial\Omega_0$, such that $\partial\Omega_0 = \partial\Omega_u \cup \partial\Omega_\sigma$.

In this analysis, it is assumed that the wave speed, $C(\varepsilon)$, depends on strain only. Furthermore, small strain theory is assumed and so mass conservation is given by

$$\rho(1 + \varepsilon) = \rho_0. \tag{17}$$

Note that under small strain assumption $\varepsilon \approx 0$ and $\rho_0 = \rho$.

Before proceeding to the method of characteristics used in this work, the shock problem will be addressed. For the clarity of the presentation, we summarize basic equations in line with the analysis presented by Tan et al. [10]. Let the location of a discontinuity be denoted by $X_s(X,t)$ (see Fig. 1). For a physical quantity ψ, the values in front of and behind the discontinuity are ψ^+ and ψ^-, respectively. The jump is defined as

$$[\![\psi]\!] = \psi^- - \psi^+. \tag{18}$$

From Hademard's Lemma, we arrive at

$$\frac{\mathrm{d}}{\mathrm{d}t}[\![\psi]\!] = \left[\!\!\left[\frac{\partial \psi}{\partial t}\right]\!\!\right] + V_s \left[\!\!\left[\frac{\partial \psi}{\partial X}\right]\!\!\right], \tag{19}$$

where $V_s = \mathrm{d}X_s/\mathrm{d}t$ is the Lagrangian wave speed. If $[\![\psi]\!] = 0$, but $[\![\partial\psi/\partial t]\!] \neq 0$, then

$$\left[\!\left[\frac{\partial\psi}{\partial t}\right]\!\right] = -V_s\left[\!\left[\frac{\partial\psi}{\partial X}\right]\!\right]. \tag{20}$$

If $\psi = u$, then (20) gives the kinematic compatibility condition,

$$[\![v]\!] = -V_s[\![\varepsilon]\!], \tag{21}$$

which is the mass flux across the shock, and indicates that it must be conserved.

The time rate of change of linear momentum must balance with the applied forces on the system. Take a control element of material located within a material layer such that $0 \le a \le b \le L$ with body forces per unit mass, f, and external force on the left, P, and on the right $P(X + \mathrm{d}X)$. From Newton's second law, we get

$$\frac{\mathrm{d}}{\mathrm{d}t}\int_a^b \rho_0 A_0 v\,\mathrm{d}X = \int_a^b \rho_0 f\,\mathrm{d}X + P(X,t)|_a^b. \tag{22}$$

Next, let two points be chosen such that $a < X_s < b$. Substitute $P = \sigma A_0$, where A_0 is the reference cross sectional area, and assume that $f = 0$, then take the limit as $a \to X_s^-$ and $b \to X_s^+$, and (22) becomes

$$-\rho_0 V_s[\![v]\!] = [\![\sigma]\!], \tag{23}$$

which is the conservation of the linear momentum across the shock.

The first law of thermodynamics states that the rate of change of the energy of a system is equal to the heat flux from the system plus the rate of work performed on the system,

$$\frac{\mathrm{d}}{\mathrm{d}t}(E_K + E_U) = \frac{\mathrm{d}Q}{\mathrm{d}t} + \frac{\mathrm{d}W}{\mathrm{d}t}, \tag{24}$$

where E_K, E_U, Q, and W are the kinetic energy, internal energy, heat of the system, and work performed on the system respectively. The energy balance on the element of material enclosed by $[a,b]$ is

$$\frac{\mathrm{d}}{\mathrm{d}t}\left(\int_a^b \rho_0\left(\frac{v\cdot v}{2} + U\right)\mathrm{d}X\right) = \underbrace{\int_a^b \rho_0 r\,\mathrm{d}X - q|_a^b}_{\text{body and surface heat}} + \underbrace{\sigma v|_a^b + \int_a^b \rho_0 f v\,\mathrm{d}X}_{\text{surface and body forces}}, \tag{25}$$

where U is the specific internal energy, r is the specific heat generation rate per unit mass, and q is the heat flux per unit area. If there is no heat generation in the element ($r = 0$), body forces are neglected ($f = 0$), and $\partial u/\partial t$ and $\partial U/\partial t$ are continuous everywhere except X_s, then (25) becomes

$$\rho_0 V_s\left[\!\left[\frac{v\cdot v}{2} + U\right]\!\right] = [\![q]\!] - [\![\sigma v]\!]. \tag{26}$$

This equation represents energy conservation. Utilizing the adiabatic assumption, (26) can be manipulated to find the change in internal energy across a shock,

$$[\![U]\!] = \frac{1}{2}\left(\sigma^- + \sigma^+\right)\frac{[\![\varepsilon]\!]}{\rho_0}. \tag{27}$$

To find the shock speed, (21) is used to eliminate $[\![v]\!]$ in (23), then solving for V_s gives

$$V_s = \sqrt{\frac{1}{\rho_0}\frac{[\![\sigma]\!]}{[\![\varepsilon]\!]}}, \tag{28}$$

which is analogous to (16). The line $[\![\sigma]\!]/[\![\varepsilon]\!]$ is the Rayleigh line, and its slope is directly related to the shock speed by (28).

Equations (21), (23) and (27) together give the change in physical states across a discontinuous wave front, Γ (see Fig. 1). These equations are equally valid in the propagation of elastic and plastic waves that are discontinuous in nature. Such waves are generally formed by sudden loading of the material on the boundaries, such as by a blast or impact.

If the jumps in (21), (23) and (27) approach infinitely small values, then the equations become the conservation conditions across a weak discontinuous wave front, which is valid within open domain $\Omega_0^{\pm}$:

$$\mathrm{d}v = \mp C(\varepsilon)\mathrm{d}\varepsilon, \tag{29}$$

$$\mathrm{d}\sigma = \mp\rho_0 C(\varepsilon)\mathrm{d}v, \tag{30}$$

$$\mathrm{d}U = \sigma\mathrm{d}\varepsilon/\rho_0. \tag{31}$$

These equations are the Method of Characteristics solution for the relationship between state variables across a wave front. Only boundary conditions that are piecewise constant will be considered meaning that Eqs. (29)–(31) evaluate trivially, thus state variables in $\Omega_0^{\pm}$ will be constant valued.

2.3. Conditions for shock formation

It is necessary to investigate the conditions under which a shock can form at a material interface. In addition to determining the necessary material properties to allow for shock formation at an interface, it is also important to investigate if the RPPL assumption is capable of properly predicting the formation of the interface shock. First, a look at a simpler elasto-plastic case will show that at an interface, for a typical set of parameters, only one plastic front or shock can form from an incident elastic wave. Two plastic waves/shock waves are possible in only a narrow range of parameters. Second, a full EPD case will be investigated to determine the criteria for shock formation in B using the results from the elasto-plastic analysis.

First consider the simpler elasto-plastic wave scenario presented in Fig. 3(a). In this case, $\varepsilon \le \varepsilon_D$. Region 0 is the initial undeformed state, region 1 is the state of the layer A after the incident wave has passed, regions 3 and 5 are the states of layer A after the reflected elastic and plastic waves pass respectively, and regions 2 and 4 are the states of layer B after the transmitted elastic and plastic waves pass respectively. At the interface velocity is continuous, otherwise the material would superimpose or open holes. Due to stress equilibrium, $\sigma_4 = \sigma_5$ in Fig. 3(a) and $\sigma_4 = \sigma_3$ in Fig. 3(b). For simplicity σ_4 will be used everywhere in derivations. As typical, it is assumed that tension is represented by positive sign and compression by negative sign. We assume for simplicity of

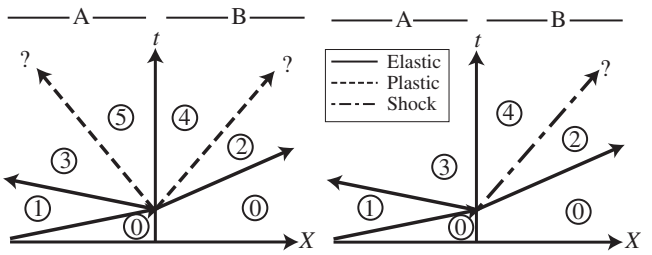

Fig. 3. Elastic wave interaction with a material interface for elastic–plastic (a) and EPD (b) material models.

discussion during the plastic analysis that the stresses are tensile. Note that the results hold for compressive stresses also.

If region 0 is at rest, then integrating (29) from 0 to 1 gives

$$v_1 - v_0 = v_1 = -\int_0^{\sigma_1} \frac{1}{\rho_0^A C^A(\sigma)} \mathrm{d}\sigma = -\frac{\sigma_1}{z^A}, \tag{32}$$

where $z = \rho_0 C$ is the elastic impedance. Note that $C\sigma$ in this context is equivalent to $C\varepsilon$. Similarly, from 0 to 2,

$$v_2 = -\frac{\sigma_2}{z^B}, \tag{33}$$

and, from 1 to 3,

$$v_3 - v_1 = \frac{\sigma_3}{z^A} - \frac{\sigma_1}{z^A}. \tag{34}$$

Since regions 4 and 5 must have equal velocities,

$$\int_0^{\sigma_5=\sigma_4} \frac{\mathrm{d}\sigma}{z^A(\sigma)} - \frac{2\sigma_1}{z^A} = -\int_0^{\sigma_4} \frac{\mathrm{d}\sigma}{z^B(\sigma)}. \tag{35}$$

Region 4 only forms if $\sigma_4 > \sigma_y^B$. Assuming this, (35) becomes

$$\frac{2\sigma_1}{z^A} = \int_0^{\sigma_4} \frac{\mathrm{d}\sigma}{z^A(\sigma)} + \frac{\sigma_4}{z_p^B} + \sigma_y^B\left(\frac{1}{z^B} - \frac{1}{z_p^B}\right), \tag{36}$$

where $z_p = \rho_0\sqrt{E_p/\rho_0}$ is the plastic impedance. If now it is assumed that $\sigma_5 = \sigma_4 > \sigma_y^A$ so that region 5 may form, then (36) becomes

$$\frac{2\sigma_1}{z^A} = \sigma_4\left(\frac{1}{z_p^A} + \frac{1}{z_p^B}\right) + \sigma_y^B\left(\frac{1}{z^B} - \frac{1}{z_p^B}\right) + \sigma_y^A\left(\frac{1}{z^A} - \frac{1}{z_p^A}\right). \tag{37}$$

Simplifying matters by assuming that $\sigma_1 = \sigma_y^A$ and solving for σ_4 gives

$$\sigma_4 = \frac{z_p^B\sigma_y^A\left(1 + \frac{z_p^A}{z^A}\right) + z_p^A\sigma_y^B\left(1 - \frac{z_p^B}{z^B}\right)}{z_p^A + z_p^B}. \tag{38}$$

If the assumption $\sigma_4 > \sigma_y^A$, is inserted in (38) it reduces to

$$\frac{\sigma_y^A}{\sigma_y^B} < \frac{1 - z_p^B/z^B}{1 - z_p^B/z^A}. \tag{39}$$

Yet, if the assumption $\sigma_4 > \sigma_y^B$ is inserted in (38) it reduces to

$$\frac{\sigma_y^B}{\sigma_y^A} < \frac{1 + z_p^A/z^A}{1 + z_p^A/z^B} \Rightarrow \frac{\sigma_y^A}{\sigma_y^B} > \frac{1 + z_p^A/z^B}{1 + z_p^A/z^A}. \tag{40}$$

After some algebra, we reach the inequality

$$\left(z^A - z^B\right)\left(z^A + z_p^A\right)\left(z^A - z_p^B\right)\left(z_p^A + z_p^B\right) < 0, \tag{41}$$

which implies that either

$$z^A > z^B \text{ and } z^A < z_p^B, \tag{42}$$

or

$$z^A < z^B \text{ and } z^A > z_p^B. \tag{43}$$

Because $z_p^B \le z^B$, the first case is not possible. Therefore, in cases where layer A is stiffer than layer B, it is not possible for both yield stresses to be less than the reflected stress. The second case leads to requirements on the differences in the yield stresses of

$$\sigma_y^A > \underbrace{\frac{1 + z_p^A/z^B}{1 + z_p^A/z^A}}_{<1}\sigma_y^B, \tag{44}$$

$$\sigma_y^A < \underbrace{\frac{1 - z_p^B/z^B}{1 - z_p^B/z^A}}_{>1}\sigma_y^B. \tag{45}$$

The range within which it is possible for both sides of the material to yield will depend directly on the plastic moduli of the materials. If $E_p^A \to 0$ and $E_p^B \to 0$ (the perfectly plastic cases) then it is impossible for two plastic waves to form even under the condition that $z^A < z^B$.

We will proceed with the assumption that $z^A > z^B$, since this case is primary focus of this work, thus only a plastic wave will form in layer B. Returning to (36), assuming that $\sigma_y^A > \sigma_4$, leads to a value for the stress in regions 4 and 5 of

$$\sigma_5 = \sigma_4 = \frac{2z_p^B\sigma_1 + z^A\left(1 - \frac{z_p^B}{z^B}\right)\sigma_y^B}{z^A + z_p^B}. \tag{46}$$

If layer B is strictly elastic, $z_p^B = z^B$, the solution reduces to the well known form of the transmitted elastic stress for a material interface

$$\sigma_5 = \sigma_4 = \frac{2z^B}{z^A + z^B}\sigma_1. \tag{47}$$

It is now established that in the case where material A is stronger (has a higher yield point) than material B, the reflected wave in layer A will be strictly elastic.

Now we investigate if a shock can form at a material interface. It is given for this part that $\sigma_y^A > \sigma_y^B$, so that, according to the previous analysis, the shock will form in layer B (see Fig. 3(b)). To ensure material equilibrium, $\sigma_3 = \sigma_4$, and from continuity, we have $v_3 = v_4$. For the incident wave, (32) is still valid. For the reflected wave,

$$v_3 = \frac{\sigma_3}{z^A} - 2\frac{\sigma_1}{z^A}. \tag{48}$$

Assuming that σ_3 is sufficient for a shock to form in layer B, the transmitted elastic wave will be at the yield point,

$$v_2 = -\frac{\sigma_y^B}{z^B}. \tag{49}$$

Note that for our material law, $E_D^B \le E^B$. Therefore, shock speed cannot exceed elastic wave speed and the shock wave will be preceded by an elastic characteristic. The jump across the shock is then

$$\sigma_3 = \sigma_y^B - \rho_0 V_s(v_3 - v_2), \tag{50}$$

and substituting for v_3 and v_2 and solving for σ_3 gives

$$\sigma_3 = \frac{\sigma_y^B z^A(1 - V_s/C^B) + 2\sigma_1\rho_0^B V_s}{z^A + \rho_0^B V_s}. \tag{51}$$

For the shock to form, assuming tensile stress, then $\sigma_D^B < \sigma_3$ gives the minimum value of V_s to be

$$V_s > \frac{C^B z^A \left(\sigma_D^B - \sigma_y^B\right)}{2\sigma_1 z^B - \sigma_y^B z^A - \sigma_D^B z^B}. \tag{52}$$

For the perfectly plastic case, $\sigma_D^B = \sigma_y^B, V_s > 0$ is the minimum shock speed, with the material condition that

$$\sigma_y^B < \frac{2z^B}{z^A + z^B}\sigma_y^A. \tag{53}$$

The result for compressive stress has the opposite inequality in (53).

To find the material properties that lead to the formation of a shock, (51) is solved instead for V_s and the constitutive law $\sigma_3 = E_D^B(\varepsilon_3 - \varepsilon_D^B) + \sigma_D^B$ is used, giving

$$V_s = \frac{C^B z^A \left(\sigma_D^B + E_D^B(\varepsilon - \varepsilon_D^B) - \sigma_y^B\right)}{2\sigma_y^A z^B - z^B\left(\sigma_D^B + E_D^B(\varepsilon - \varepsilon_D^B) - \sigma_y^B\right) - \sigma_y^B z^A}. \tag{54}$$

Since $V_s > 0$, and z^A, $z^B > 0$, either both the numerator and denominator are positive or both are negative. For the numerator, the condition must hold that

$$\sigma_D^B + E_D^B\left(\varepsilon - \varepsilon_D^B\right) \gtrless \sigma_y^B, \tag{55}$$

where $>$ indicates tensile stress and $<$ indicates compressive stress. Since the material behavior is defined such that the $\sigma_D^B > \sigma_y^B$ for tensile stresses and $\sigma_D^B < \sigma_y^B$ for compressive stresses, this is automatically satisfied. For the denominator,

$$2\sigma_y^A \gtrless \sigma_D^B + \sigma_y^B\frac{z^A}{z^B} + E_D^B\left(\varepsilon - \varepsilon_D^B\right), \tag{56}$$

again where $>$ indicates tensile stress and $<$ indicates compressive stress. Since both cases are analogous, attention will be given only to the positive case. The term $E_D^B(\varepsilon - \varepsilon_D^B)$ corresponds to the additional stress resulting from the shock that is beyond the densification stress, σ_D^B, this stress will be referred to as "residual shock stress". For residual shock stress to occur,

$$2\sigma_y^A > \sigma_D^B + \sigma_y^B\frac{z^A}{z^B} \tag{57}$$

must hold, and the amount of residual stress corresponds to the magnitude of the difference. If $-z^A v_1$ is substituted for σ_y^A then

$$-v_1 > \frac{\sigma_D^B}{2z^A} + \frac{\sigma_y^B}{2z^B}, \tag{58}$$

which gives the necessary velocity in region 1 to lead to a shock. If layer A is modeled as an RPPL material so that $z^A = \infty$, (58) reduces to

$$-v_1 > \frac{\sigma_y^B}{2z^B}, \tag{59}$$

giving a finite, non-zero, value for v_1. However, $v_1 = -\sigma_y^A/z^A = 0$, meaning that (59) cannot be satisfied. This implies that the multilayer material problem cannot be appropriately solved while using an RPPL model.

For completeness, the minimum velocity to be applied to the free end of layer A that generates a shock in layer A is now investigated. If v_0 is the boundary applied velocity, then

$$v_0 = -\int_0^{\sigma} \frac{1}{\rho_0^A C^A(\sigma)}\mathrm{d}\sigma. \tag{60}$$

The maximum velocity, $v_{\max}$ that will not generate a shock is the one that raises the stress in the material up to the densification stress. Thus, if $\sigma = \sigma_D^A$, then

$$v_{\max} = -\frac{\sigma_D^A - \sigma_y^A}{\rho_0^A V_p} - \frac{\sigma_y^A}{\rho_0^A C^A}, \tag{61}$$

where

$$V_p = \sqrt{\frac{1}{\rho_0^A}\frac{\sigma_D^A - \sigma_y^A}{\varepsilon_D^A - \varepsilon_y^A}}. \tag{62}$$

Thus the velocity condition for the formation of a shock at the left boundary is $v_0 > v_{\max}$.

2.4. Numerical implementation

It is first noted that the assumption of piecewise constant boundary conditions enforces that all wave fronts are at least weakly discontinuous and that the regions between wave fronts are constant. This means that (21), (23) and (27) can be used to solve all wave interactions. This greatly simplifies the computational implementation since no numerical integration across wave fronts is necessary.

All wave interactions, whether with a boundary, an interface, or a wave collision, are analyzed as a two-wave collision at an interface using method of characteristics, Eqs. (29)–(31). Thus at the interaction point there will be a Left (L) side and a Right (R) side and a wave coming from each direction with known stress, strain, velocity, and internal energy. When the two waves collide, they may transmit one or two waves and/or reflect one or two waves. What happens depends on the strength of the incoming waves and the materials associated with the L and R sides. In the case of boundaries, one side is either an infinitely stiff material (fixed end condition) or an infinitely soft one (free end). This defines the stress (or velocity) of the reflected wave and allows for the same solution method to be used.

In each interaction the state ahead of the incoming waves is known. The problem is to solve for the central stress σ_c and central velocity v_c between the transmitted and reflected waves. Equilibrium and continuity demands that the stress and velocity between transmitted and reflected waves be the same, thus (23) can be used on both the L and R sides and then combined to solve for the central velocity,

$$v_c = \frac{\sigma^R - \sigma^L + \rho_0^L V^L v^L + \rho_0^R V^R v^R}{\rho_0^L V^L + \rho_0^R V^R}, \tag{63}$$

where V, v, σ, ρ_0 are the wave speed material speed, stress, and density of the respective collision sides. The stress can be found from (23) using either side as

$$\sigma_c^R = \sigma^R - \rho_0^R V^R\left(v_c - v^R\right), \tag{64}$$

$$\sigma_c^L = \sigma^L + \rho_0^R V^L\left(v_c - v^L\right). \tag{65}$$

For the converged solution, $\sigma_c^R = \sigma_c^L = \sigma_c$. To find the correct central stress, the correct wave speeds are found through an iterative procedure that operates on both L and R halves. First the central stress is guessed (in the case of a boundary reflection, this value is known). A good initial guess is found from (63) and (65) with the assumption that the wave speeds are elastic, i.e., $V^L = C^L$ and $V^R = C^R$. The central stress is then compared against the yield point, Eq. (7), of the given half. If the stress does not cause the

material to yield, then new velocity, and strain values are calculated from (23) and (21).

For material that flows plastically, the yield condition is calculated. We introduce an iterative process where subscript n represents the incoming state (either L or R), and $n+1$ represents the final converged state. The yield condition, Eq. (7), takes the incremental form

$$f_{n+1} = |\sigma_{n+1}| - \left[\sigma_y + \vec{H}\cdot\left(\vec{\alpha}_n + \overrightarrow{\Delta\gamma}\right)\right], \tag{66}$$

where $\Delta\gamma$ is the yield step and is obtained from the consistency condition, $\dot{\gamma}_{n+1}\dot{f}_{n+1} = 0$. Since the material has multiple hardening moduli, $k = 1,2$, each $\Delta\gamma^k$ is calculated separately as

$$\Delta\gamma^k = \frac{|\sigma_{n+1}| - \left(\sigma_y + H^k\cdot\alpha_n^k\right)}{H^k}. \tag{67}$$

The step is then compared against the maximum value of α^k to see if the material has yielded beyond the limit of the current material branch. If it has, then $\Delta\gamma^k$ is truncated to the limit and then (67) is recalculated for $k+1$. This process is repeated until $\Delta\gamma^k$ does not exceed the length of its current hardening branch. The yield point is updated, $\alpha_{n+1}^k = \Delta\gamma^k + \alpha_n^k$, and the plastic strain is updated, $\varepsilon_i(n+1) = \varepsilon_i(n) + \sum_{k=1}^{2}\Delta\gamma^k \mathrm{sign}(\sigma_{n+1})$. The total strain is then found from Eq. (6).

Next the wave speeds, V^L and V^R, are recalculated from (28) using the σ_{n+1} and ε_{n+1} values of the respecitve halves. A new v_c is calculated from the new wave speeds using (63) and then new σ_c^R and σ_c^L are updated from (65). The process is repeated until the change in $\sigma_c^R = \sigma_c^L = \sigma_c$ from one iteration to the next is below the tolerance, $|\sigma_c(j+1) - \sigma_c(j)| < 1\times10^{-4}$ Pa, where j represents the iteration number. Last, internal energy is found from (27).

3. Numerical examples

3.1. Model verification

It is critical to verify the present implementation. We use the work of Harrigan et al. [20] for the verification study. This work utilizes a single-layer bar of Rohacell 1 m in length which is fixed on the right end and free on the left end. A constant stress of 3.6 MPa is applied to the free end for 1.53 ms. Harrigan uses two material models, an RPPL and an elastic-perfectly-plastic-hardening (EPPH) material model. Since the EPPH model is similar to the EPD model used in this work, it serves as a good comparison. The main difference between the EPD and EPPH models is that Harrigan uses the EPPH model for un-densified regions only. Regions that have been compacted by a shock front are afterward treated using the RPPL model. The primary result of this difference is that once the load is released, the shock front immediately begins to unload. This means that there is no lag time between the onset of unloading and when the unloading wave reaches the shock front, as shown in what follows.

Table 1 contains the material parameters used in Harrigan et al. [20] and the present work. The strain in the EPPH densification region is calculated from

$$\varepsilon = \frac{k^2(\sigma-\sigma_y) + 2\varepsilon_D\rho_0 + k\sqrt{\sigma-\sigma_y}\sqrt{k^2(\sigma-\sigma_y) + 4(\varepsilon_D-\varepsilon_y)\rho_0}}{2\rho_0} > \varepsilon_D, \tag{68}$$

where $k = 0.00105$. Fig. 4(a) shows excellent agreement between the two material laws.

Table 1
Material data for EPD verification comparison.

	ρ_0 [kg m^{-3}]	E [MPa]	E_D [MPa]
EPPH	51.6	22.0	N/A
EPD	51.6	22.0	17.6
	$\sigma_y = \sigma_D$ [MPa]	ε_y [%]	ε_D [%]
EPPH	0.8	3.64	68.9
EPD	0.8	3.64	75.7

The present EPD model was run for both a limit scenario ($E = E_D = 22$ GPa, $H_2 = \infty$) and the scenario given in Table 1. In the limit case, the densification strain was set at 68.9%. It is clear from Fig. 4(b) that the RPPL and limit EPD models produce nearly an exact match.

As expected, the EPD model (solid line with circles in Fig. 4(b)) takes longer to dissipate the shock than Harrigan's EPPH model. This is due to the RPPL assumption in compacted regions. There is a delay of nearly a millisecond as the unloading wave catches up to the shock front. Thus the shock front is not dissipated as quickly. Furthermore, Fig. 5 reveals that the reflected shock wave and the incoming shock front collide (depicted by dash-line circle in Fig. 5), resulting in a region of higher stress at the back wall at $t = 7$ ms, which is not predicted by the EPPH model. This difference in stress highlights the importance of full elastic modeling of the material. The initial shock speed in this loading scenario is $V_s = 248.3$ m/s and the speed of the reflected shock is $V_s = 32.9$ m/s.

3.2. Two layer analysis

To better understand the behavior of two-layer systems, an investigation of a two-layer system is conducted. The boundary and loading conditions are the same as in the previous section with the 1 m foam rod now divided in half to form a two-layer system. The density combination $\rho_0^A > \rho_0^B$ was chosen so that it is possible for both layers to yield. If the second layer is more dense (and hence stiffer), then it will not generate a shock or plastic wave unless the first layer has fully collapsed and there is sufficient velocity left in the first layer to propagate the shock further (see Section 2.3). Table 2 displays the material parameters used for this analysis.

For the two layer analysis, the shock energy exceeds the elastic contribution as depicted in Fig. 6. Fig. 7(a) shows that the energy behind the shock in A is larger than that in B. Spalling would occur around 2 ms (see Fig. 7(b)). The strains behind the initial shock fronts in A and B are $\varepsilon^A(X = 0, t = 0.5) = -0.59896$ and $\varepsilon^B(X = 50, t = 1) = -0.69049$ (strains are constant for the whole region). The strain behind the reflected shock front from the distal boundary is $\varepsilon^B(X = 100, t = 2) = -0.6904$.

The shock front in B speeds up briefly from $V_s = 37.2$ m/s at $t = 1.60$ ms to $V_s = 104.2$ m/s at $t = 1.71$ ms from the elastic reflection of the shock front in layer A (at $\approx$1 ms). The shock then terminates at $t = 2.14$ ms, reforming briefly as a plastic wave at $t = 2.35$ ms and then again as a shock at $t = 2.94$ ms. The unloading wave that initially terminates the shock formed at the interface in layer B also weakens the reflected shock, reducing it to a strictly plastic wave. The maximum shock speed in layer A is $V_s^A = 133.5$ m/s, and in layer B is $V_s^B = 104.2$ m/s.

4. Optimization

For the optimization section, the boundary conditions will continue to be fixed on the right end and free on the left end of the beam. The load pulse magnitude used is $\bar{t} = 3.6$ MPa and the loading pulse duration is reduced to 100 μs. For simplicity, the reference cross sectional area will be treated as unity, $A_0 = 1$ cm^2.

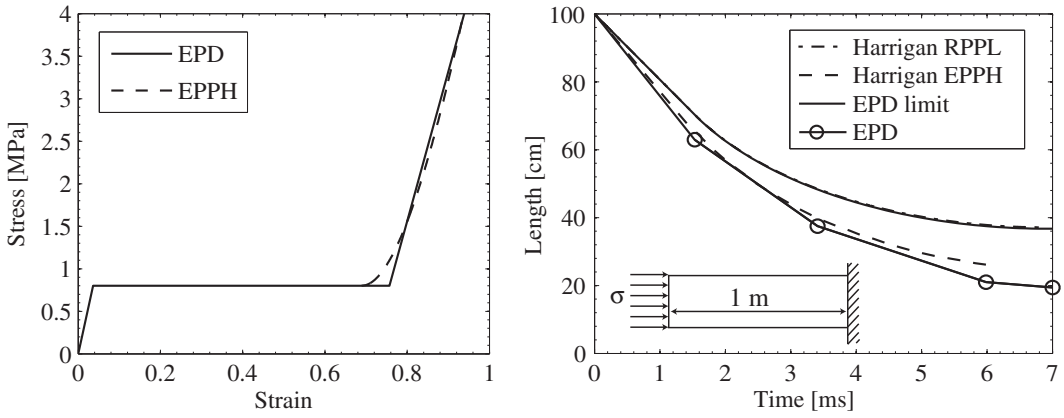

(a) EPD and EPPH material laws. (b) Front face deformation of foam column.

Fig. 4. Comparisons of material laws (a) and front face deformations (b). Data for RPPL and EPPH are taken from [20].

The base material of Rohacell foam, used for this section, is polymethacrylimide (PMI), and has density $\rho_0^s = 1.2$ gm/cm^3, yield stress $\sigma_y^s = 90$ MPa, and elastic modulus $E^s = 5.2$ GPa.

4.1. Objective function

Cellular materials are used to protect objects and prevent damage. This purpose drives the development of constraints and objective functions for our optimization. In protective applications, the objective is usually to keep transmitted loads below some limit. In terms of an optimization, the problem can be cast either as a minimization of transmitted load or as a function of some other important parameter with the transmitted load applied as a constraint. Since weight and/or volume are important considerations for a protective layer, especially in armor design, the optimization problem is usually proposed as a minimization of either of these parameters and load transmission is added as a constraint.

For the present work, the objective will be to minimize total length of the protective system. Thus the problem is to find a length that appropriately mitigates expected damage quantities. The constraint is cast as a limit on the maximum impulse transmitted to the protected object. Impulse is written in terms of acceleration or applied stress as

$$I = MGg\cdot(t_2 - t_1) = A_0 \int_{t_1}^{t_2} \sigma \mathrm{d}t, \tag{69}$$

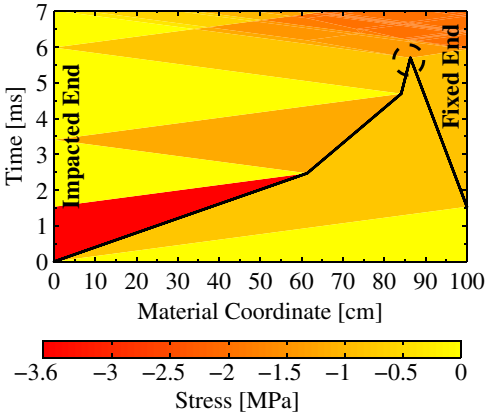

Fig. 5. EPD stress contours. Bold solid lines indicate the positions of shock waves.

where M is the mass of the protected object, G is a gravity multiplication factor and $g = 9.81$ m/s^2 is the acceleration due to gravity. In occupant protection scenarios, there is a limit on the number of G's that a person can handle without fatal injury. Values used by the U.S. Military can be found in [43]. In the current work, since a fixed boundary condition is used on the distal end, it is necessary to convert any acceleration derived impulse into its equivalent stress value. In this work, we select a stress limit of $\sigma_{\max} = 1$ MPa. In a real world scenario, G, M, and A_0 will be known or design values and the stress can be calculated from them.

To compare one and two layer systems, we also discuss a mass constraint. Since the applied load is a fixed pulse, the amount of energy put into the system will depend on the total deformation of the system, which is a function of the relative mass densities and stiffnesses of the layers. With mass and impulse constraints considered, the optimization problem can be written as

$$\min\left(L^A + L^B\right), \tag{70}$$

$$s.t.\ \frac{1}{t_2 - t_1}\int_{t_1}^{t_2} \sigma\left(L^A + L^B, t\right)\mathrm{d}t < \sigma_{\max}, \tag{71}$$

$$M_{\mathrm{tot}} = M^A + M^B < M^*, \tag{72}$$

where M^A and M^B are the layer masses and M^* is the mass of the single layer optimum. The impulse constraint width $t_2 - t_1$ can be varied to restrict or relax the constraint and is applied as a sliding window over the distal stress. In this work the relaxed constraint is $t_2 - t_1 = 40$ μs and the strict constraint is $t_2 - t_1 = 10$ μs.

Table 2
Material data for two layer analysis.

Material	A	B
ρ_0 [kg m^{-3}]	110.0	51.6
E [MPa]	67.37	22.0
E_p [MPa]	0.67	0.022
E_D [MPa]	67.37	22.0
σ_y [MPa]	2.5	0.8025
σ_D [MPa]	2.87	0.8169
ε_D [%]	58.81	68.9

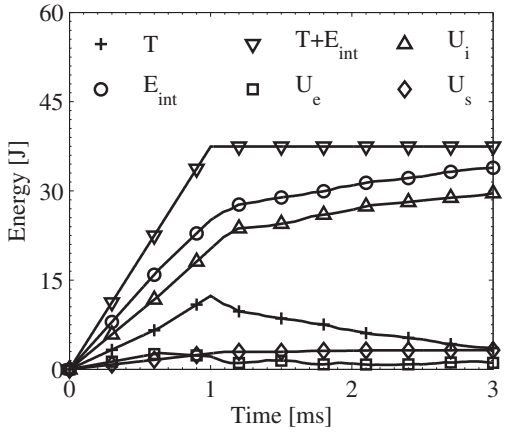

Fig. 6. Kinetic and internal energy for two layer analysis. U_e is the elastic energy, U_i is the inelastic energy and U_s is the additional inelastic energy contributed by the shock waves in the material. $E_{\text{int}} = U_e + U_i + U_s$ is the total internal energy. T is the kinetic energy.

4.2. Non-linear sensitivity analysis

To select design variables, the material properties which influence the distal stress are determined. Note that we do not consider any distal impulse constraint in the non-linear sensitivity study.

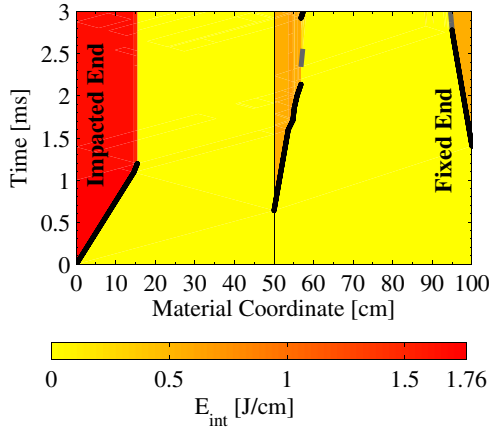

(a) Contours of E_{int}.

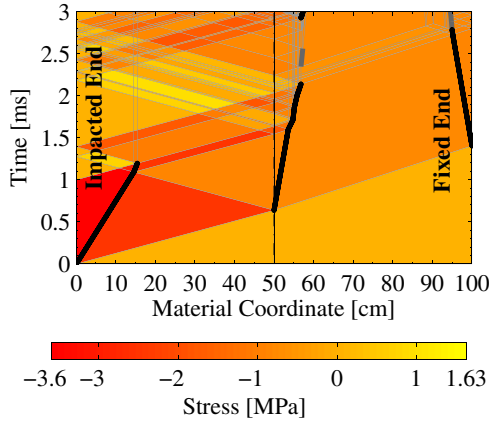

(b) Stress contours.

Fig. 7. Two layer analysis. The plastic waves are indicated by bold gray lines for $\Delta\sigma > 0.01$ MPa and shocks are indicated by bold black lines for $[\![\sigma]\!] > 0.01$ MPa. Wave reflections are indicated by thin gray lines. Thin vertical black line indicates material interface.

Earlier it was established that the material properties of a cellular material are functions of the relative density (see Section 2.1). If we further constrain $E_D = E$, which approximates actual cellular compressive behavior [8], there are only three independent quantities to consider per layer: $\overline{\rho}_0$, E_p or H_1, and L, for a total of six.

Since the problem is highly non-linear, a full factorial design of experiments study is conducted to determine the sensitivity of the problem to each of the six parameters. Fig. 8 shows the average of the standard deviations of the impulse at the distal end for each of the parameters. Standard deviation is taken over a triplet and the average is taken over all the triplets for a given parameter. A triplet is a set of low-mid-high values for the given parameter, where all other parameters are held constant. The most influential parameter is the relative density of the distal layer (layer B). This is because the density of layer B directly affects σ_y^B, which has the most immediate influence on the reflected stress at the fixed wall. The plastic modulus of A has a negligible effect on the distal stress. This is because A receives the impulse and immediately shocks along the Rayleigh line, which completely bypasses the plastic branch of the material. The plastic modulus of B is more significant because it has a direct influence on the value of the stress reflected off the distal end. There is no significant correlation when parameters are analyzed as a coupled pair (e.g. $\overline{\rho}_0^A$ and E_p^A are analyzed together).

4.3. One layer optimization

A one layer baseline establishes an upper bound for the total two layer length, L_{tot}, as well as the mass constraint, M^*. Using the three design parameters, $\overline{\rho}_0$, E_p, and L, a study was conducted to find the minimum length for a single foam layer using PMI as the base material. Defining areal impulse to be $I' = I/A$, a stress of 1 MPa applied over a time width of 10 μs is used to give the areal impulse constraint ($I' = 10$ MPa μs). The maximum $\overline{\rho}_0$ which will not exceed the stress constraint upon reflection off the distal boundary is calculated using the method discussed in Section 2.4. The value of maximum density, assuming $E_p = 0$, is $\overline{\rho}_{\max} = 0.04794$, and it is the boundary of the design space. If either $\overline{\rho}_0 > \overline{\rho}_{\max}$ and $E_p = 0$ or $\overline{\rho}_0 = \overline{\rho}_{\max}$ and $E_p > 0$ the stress constraint will be violated for all lengths. The value of $E_p = 0.2$ MPa is the maximum allowable plastic modulus that will not violate the stress constraint upon the initial reflection off the distal boundary for the case where $\overline{\rho}_0 = 0.047$. The $\overline{\rho}_0 = 0.048$ case, at $I' = 10.01$ MPa μs, will just violate the constraint. Thus, the $\overline{\rho}_{\max}$ case provides the minimum value, $L_{\min} = 6.64$ cm. Note that reducing the density, regardless of E_p, increases the distal stress. The reason for this behavior is that lower density materials have a lower yield stress, which means that the total plastic dissipation is less and so more length is needed to provide the same total energy dissipation. Increasing the plastic modulus does not eliminate the deficit in energy dissipation and increases the stress of the initial reflection.

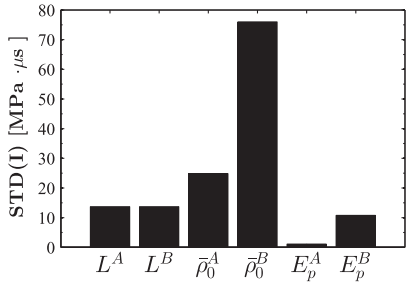

Fig. 8. Sensitivity of distal stress to each design parameter. Y-axis is the average of the standard deviations of each parameter triplet. A triplet is a set of low-mid-high values for the given parameter where all other parameters are held constant.

Fig. 9(a) shows the system energies for the $\overline{\rho}_0 = 0.04794$ one-layer optimum point for a $t_2 - t_1 = 10$ μs impulse width. The shock contribution to energy dissipation is 46.6%. Fig. 9(b–d) shows the internal energy, stress, and velocity contours. At $t = 0.16$ ms, when the unloading wave first catches the shock wave, 79.1% of the total system energy has been dissipated. At this time, the dissipation rate is reduced by the decrease in the shock strength from $V_s = 249.2$ m/s to $V_s = 90.0$ m/s, which is seen in Fig. 9(b) by the change in color of the internal energy from red to orange after the reflection of the unloading wave. The second collision of the unloading wave at $t = 0.30$ ms reduces the shock speed to $V_s = 2.54$ m/s, and at this time 94.8% of the energy is dissipated. After the termination of the shocks at $t = 0.46$ ms, 0.4% of the energy remains as elastic energy. Note that the incoming and reflected shocks do not collide, instead they are terminated by the unloading wave just prior to collision. The termination prevents a region of high stress from forming (see Fig. 5 and the discussion in section 3.1) and allows the impulse constraint to be satisfied for all time. This length fully utilizes all of the available material for energy dissipation. Finally, the velocity contours indicate the material is nearly at rest when the shocks terminate, but remaining elastic energies cause the densified material to oscillate between positive and negative velocities.

4.4. Two layer optimization

To better visualize the design space, we perform an exhaustive search within the design region. Thus the two layer optimization was conducted in two phases, where Phase 1 is a coarse grain search and Phase 2 is a refined search over a reduced space based on the results of the first search. The impulse constraint is the same as in the single layer case (strict constraint) for both phases. However, we add the relaxed constraint during Phase 2 for comparison.

Phase 1 optimization. Design variables for the first phase were varied according to the values in Table 3. The ranges were chosen to give good coverage of the design space. Note if $\overline{\rho}_0^A > 0.117$ no plasticity will occur in layer *A*. For each value of L^A a binary search for the minimum value of L^B was conducted with a termination on the change in length of $|L_{n+1}^B - L_n^B| < 0.1$ cm. The results of this phase show that there are no successful points off of the $\overline{\rho}_0^B = 0.04794$ and $E_p^B = 0$ boundary, confirming the observation from the single layer optimization. Although $\overline{\rho}_0^B$ was reported to have the most influence on the distal stress (see Section 4.2), for purposes of determining the optimum, the results of the one layer and phase 1 optimizations show that it should not be included as a design variable. An increase in $\overline{\rho}_0^B$ will exceed the impulse constraint while a decrease will not fully utilize the dissipative capabilities of layer *B*. This is due to the very high sensitivity of distal stress on $\overline{\rho}_0^B$ as shown in Fig. 8. Similarly, varying E_p^B is also not necessary. Having a value of $E_p^B > 0$ forces $\overline{\rho}_0^B < 0.04794$ and therefore does not maximize the dissipative potential of layer *B*. Therefore, for Phase 2, $\overline{\rho}_0^B = 0.04794$ and $E_p^B = 0$ become fixed quantities.

Phase 2 optimization. The remaining design variables for phase 2 are $\overline{\rho}_0^A$, L_A and L_B. $\overline{\rho}_0^A$ was varied from 0.06 to 0.15 by 0.03 increments. The density range was selected based on the relative densities of Rohacell foam currently available, which range from 0.043 to 0.171 [44]. L^A was varied from 0.4 to 5.0 cm by 0.2 cm increments. L^B was

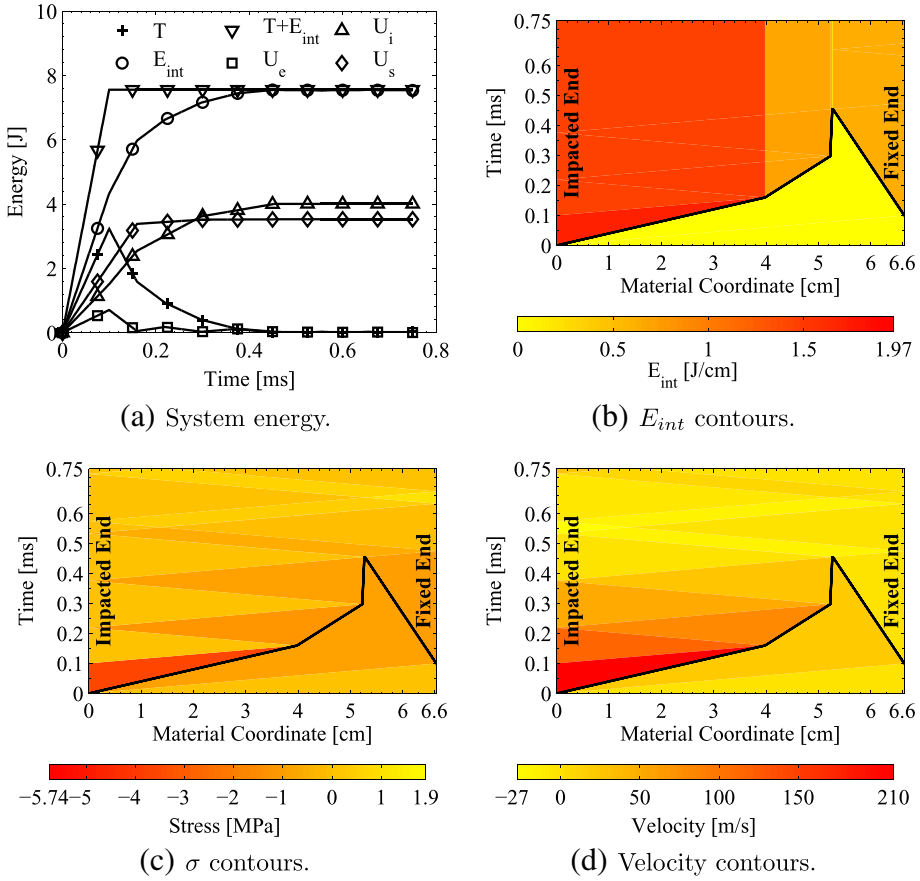

(a) System energy. (b) E_{int} contours. (c) σ contours. (d) Velocity contours.

Fig. 9. Evolution of energy quantities, as well as internal energy, stress, and material velocity contours for the optimal length of a single layer foam for $\overline{\rho}_0 = 0.04794$, $E_p = 0$, and impulse width constrained at $t_2 - t_1 = 10$ μs.

Table 3
Material data for phase 1 optimization.

Property	$\overline{\rho}_0$	E_p	L
Layer A	0.05, 0.08, 0.12, 0.15	0 MPa	0.5–6.0 cm
Layer B	0.046, 0.047, 0.04794	0, 0.1, 0.2 MPa	$L_B < 6.64 - L_A$ cm

decreased from the maximum $L^B = L_{\max} - L^A$ by 0.1 cm increments until the impulse constraint could not be satisfied, where $L_{\max} = 6.64$ cm (one layer optimum length).

Fig. 10 shows $L_{\text{tot}}/L_{\max}$ for each of the tested values of $\overline{\rho}_0^A$ as a function of L^A. Black marker-lines are below the one-layer mass limit ($M^* = 0.382$ g) while gray marker-lines are above it. Missing data points are unable to satisfy the impulse constraint for any value of $L^B + L^A < L_{\max}$.

In Fig. 10(a), the relaxed, $t_2 - t_1 = 40$ μs, impulse constraint is used. The minimum for each curve is closer to the lower end of the design space. It is the stiffest material, $\overline{\rho}_0^A = 0.015$, for which layer A remains entirely elastic, that gives the global minimum total length at $L_{\min} = 4.54$ cm with $L^A = 1.6$ cm.

Fig. 10(b) shows the results when the strict, $t_2 - t_1 = 10$ μs, constraint is applied. In general, there is greater difficulty in satisfying the impulse constraint as is indicated by the increase in missing data points (due to the constraint violation) and the non-monotonic curve profiles. Note that in some cases, e.g., $\overline{\rho}_0^A = 0.15$ and $\overline{\rho}_0^A = 0.12$ cases, multiple points have the same minimum total length. However, the optimum is still on the $\overline{\rho}_0^A = 0.15$ curve, now at 4.64 cm and $L_A = 1.4$ cm. The optima for the $\overline{\rho}_0^A = 0.06, 0.09, 0.12$ curves are $L_{\text{tot}} = 6.14$ cm, 5.44 cm, and 5.24 cm for $L^A = 1.8$ cm, 2.2 cm, 1.2 cm, respectively. The optimal points are indicated by black filled marker faces and labeled A, B, C, and D in Fig. 10(b). The points listed are the ones with the least mass among equal length minima. Finally, although the minimum is much lower for the $\overline{\rho}_0^A = 0.15$ case than all the others, if a mass constraint is applied (black line and marker edges), the reduction in total length from the $\overline{\rho}_0^A = 0.12$ to the $\overline{\rho}_0^A = 0.15$ case is only 0.1 cm. Note that only for the $\overline{\rho}_0^A = 0.06$ case, the minimum length also satisfies the mass constraint of the one layer optimum. However, for all the cases, large length reductions, with respect to the one layer case, are still obtained without increasing the mass (7.5% for $\overline{\rho}_0^A = 0.06$, 12.4% for $\overline{\rho}_0^A = 0.09$, 18.4% for $\overline{\rho}_0^A = 0.12$, and 19.9% for $\overline{\rho}_0^A = 0.15$). The minima data points A, B, C, and D are investigated in more detail next.

Case A($\overline{\rho}_0^A = 0.06$): From Fig. 11(a), we can see that the shocks contribute to nearly 34% of the total dissipation and Fig. 11(b) indicates that both layers are responsible for a significant portion of the energy absorption. Note that all of the material undergoes compaction by the final stage. Additionally, the mass of this design, $M_{\text{tot}} = 0.378$ g, is lower than that of the single layer system ($M^* = 0.382$ g). Of interest is the set of shock waves that form between the incoming and reflected shock waves at $X = 5.1$ cm and $t = 0.30$ ms. These waves form when the incoming shock temporarily disappears due to a tensile wave catching up with the front followed shortly by a compaction wave. When the tensile wave reflects off the distal shock it does so in compression. Then, when the tensile wave's reflection encounters the incoming compression wave, they collide and exceed the densification point. The shock in layer B varies widely in speed, reaching a peak of $V_s = 245.9$ m/s at $t = 0.15$ ms, after layer A collapses. The maximum shock speed in layer A is $V_s = 216.5$ m/s. A tensile wave forms in layer A around $t = 0.12$ ms, which would result in spalling (see Fig. 11(c)). The tensile wave does not reach the shock, but temporarily reduces compressive stress, slowing the shock front in layer B between $t = 0.15$ ms and $t = 0.17$ ms to as little as $V_s = 21.5$ m/s before speeding up to $V_s = 110.4$ m/s. The minimum strains (maximum compressive strains) are $\epsilon^A_{\min} = -0.7727$ and $\epsilon^B_{\min} = -0.8176$ in layers A and B respectively.

Case B($\overline{\rho}_0^A = 0.09$): Fig. 12 reveals that a significant portion of layer A is not compacted. Additionally, the stresses in layer B remain low behind the shock fronts. Together, the higher density of A (and thus higher σ_y^A) and lower stresses in B lead to a reduced contribution to energy dissipation by the shocks (12.1%). The mass, $M_{\text{tot}} = 0.424$ g, exceeds the one layer case by 11.0%. This system is shorter than the $\overline{\rho}_0^A = 0.06$ case by 0.7 cm with $L_{\text{tot}} = 5.44$ cm. The additional mass in A that is uncompacted acts as an inertia buffer thus allowing shorter lengths of layer B. The higher elastic wave speed in layer A leads to a greater number of reflections off of the material interface, which in turn leads to a more smoothly varying shock front in layer B as more waves interact with it. The maximum shock speeds are $V_s^A = 137.7$ m/s and $V_s^B = 133.7$ m/s in layers A and B respectively. The minimum strains are $\epsilon^A_{\min} = -0.6257$ and $\epsilon^B_{\min} = -0.7239$ in layers A and B respectively.

Cases C and D($\overline{\rho}_0^A = 0.12$ and $\overline{\rho}_0^A = 0.15$): Because layer A does not deform plastically in either Case C or Case D, the results are qualitatively similar. Therefore, we describe in detail Case C only. Since the first layer remains elastic, there is no energy dissipation provided by layer A as shown in Fig. 13(b). The shock contribution to

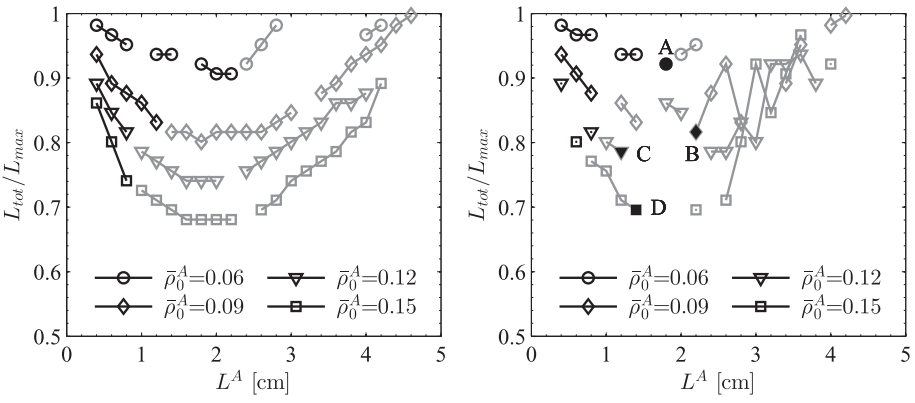

(a) $t_2 - t_1 = 40\mu$s. (b) $t_2 - t_1 = 10\mu$s.

Fig. 10. Curves of non-dimensional optimal length as a function of L^A. Missing data points indicate that no value of L^B for that length of L^A could satisfy the impulse constraint. Gray points indicate that the solution violates the mass constraint. Filled in markers, for the $t_2 - t_1 = 10$ μs case, are minimum total length points. A non-dimensional length of $L_{\text{tot}}/L_{\max} = 1$ corresponds to the one layer optimum $L_{\max} = 6.64$ cm.

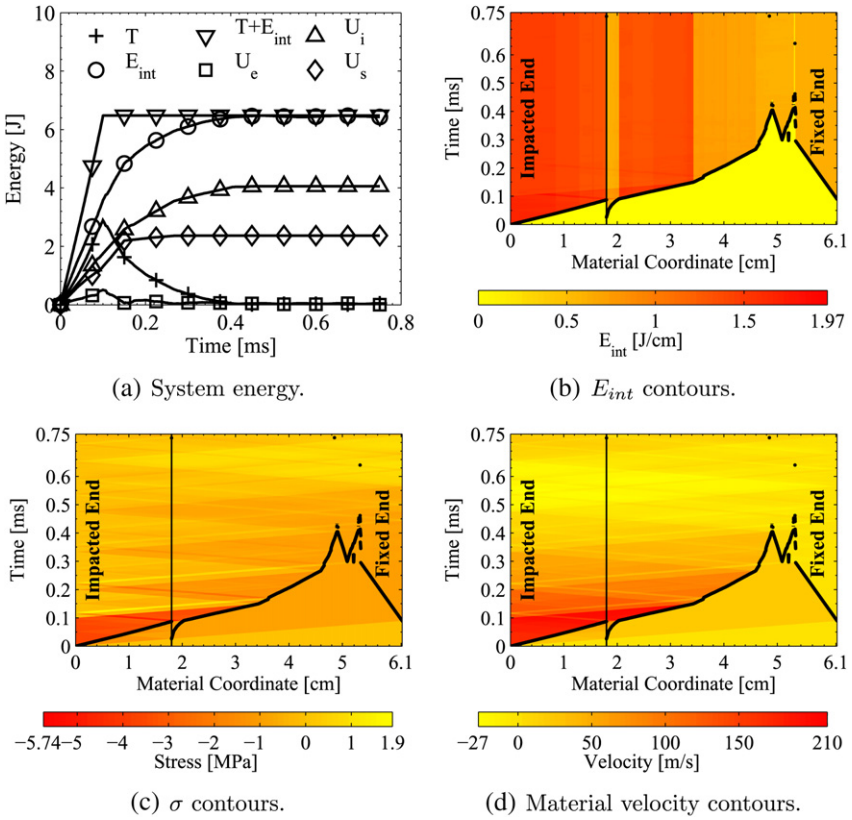

(a) System energy. (b) E_{int} contours.

(c) σ contours. (d) Material velocity contours.

Fig. 11. Evolution of energy quantities, as well as internal energy, stress, and material velocity contours for the optimal length of L^B for $\bar{p}_0^A = 0.06$, point A in Fig. 10(b), and impulse width constrained at $t_2 - t_1 = 10$ μs. Thin vertical black line indicates material interface.

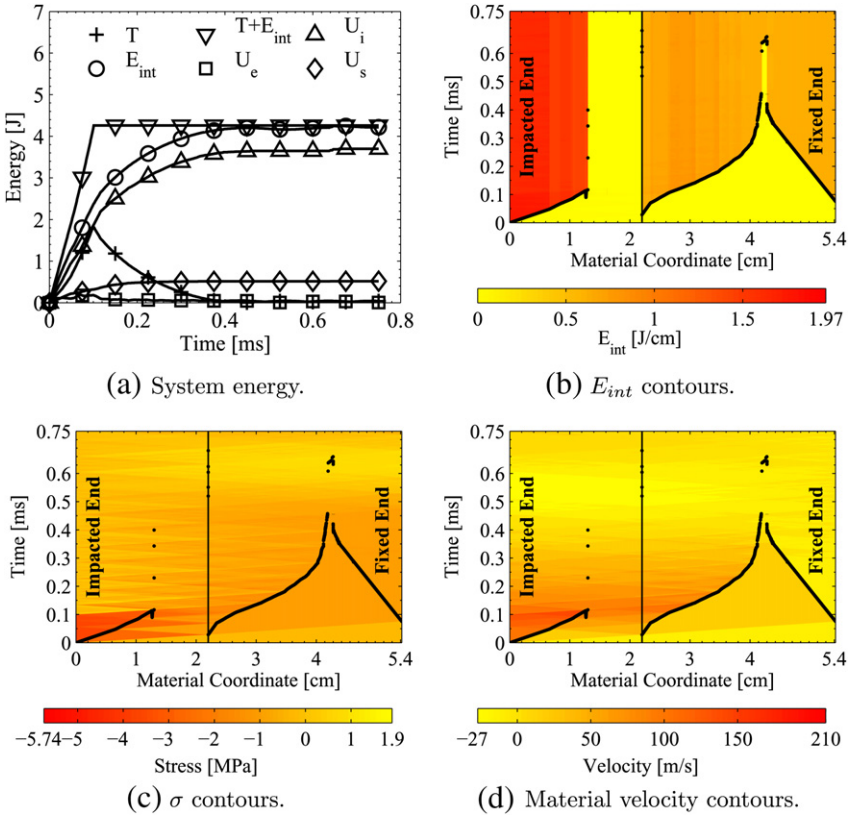

(a) System energy. (b) E_{int} contours.

(c) σ contours. (d) Material velocity contours.

Fig. 12. Evolution of energy quantities, as well as internal energy, stress, and material velocity contours for the optimal length of L^B for $\bar{p}_0^A = 0.09$, point B in Fig. 10(b), and impulse width constrained at $t_2 - t_1 = 10$ μs. Thin vertical black line indicates material interface.

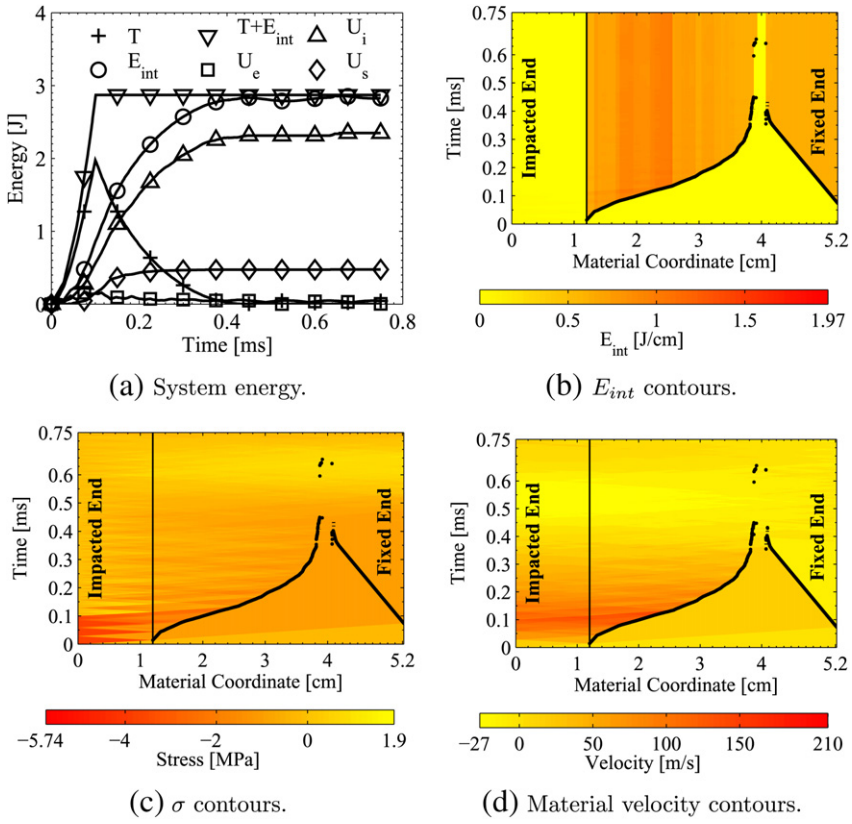

Fig. 13. Evolution of energy quantities, as well as internal energy, stress, and material velocity contours for the optimal length of L^B for $\overline{p}_0^A = 0.12$, point C in Fig. 10(b), and impulse width constrained at $t_2 - t_1 = 10$ μs. Thin vertical black line indicates material interface.

energy dissipation is 16.5%. However, since layer A is stiff and the total bar deformation is small, the amount of input energy is low, and thus layer A does not require as much material in layer B to dissipate the loading pressure pulse. The shock speed increases with each reflection off the material interface from the waves in layer A during the loading period ($t < 0.10$ ms). The internal energy amount grows larger as V_s increases (indicated by flattening of the bold shock line) from $V_s = 41.2$ m/s to a maximum of $V_s = 184.3$ m/s, when the unloading wave reaches the front and the speed begins to decrease. Fig. 13(d) shows that the material velocity takes time to ramp up prior to the end of the load pulse. Layer A operates strictly as an inertia buffer, delaying the ramp up in material speed with its own mass. Once the loading pulse ends, the velocity ramps down to elastic speeds. The mass of Case C is $M_{\text{tot}} = 0.405$ g, which exceeds M^* by 6.0%. The minimum strains are $\epsilon^A_{\text{min}} = -0.0347$ and $\epsilon^B_{\text{min}} = -0.7399$ in layers A and B respectively. Note the small elastic compressive strain in layer A.

The primary difference in Case D is that layer A is 0.2 cm longer and the total energy is 2.09 J as opposed to 2.87 J in Case C. The shock contribution to energy dissipation reduces to 9.4% in Case D, and the shock speed increases from $V_s = 21.5$ m/s to a maximum of $V_s = 144.1$ m/s. The mass of Case D is higher than Case C at $M_{\text{tot}} = 0.438$ g, which exceeds M^* by 14.7%. The minimum strains are $\epsilon^A_{\text{min}} = -0.0270$ and $\epsilon^B_{\text{min}} = -0.7236$ in layers A and B respectively.

Fig. 14 shows the position of the front end and the material interface for the one layer case and cases A through D. In Case A ($L_{\text{tot}} = 6.14$) layer A collapses from $L^A_0 = 1.80$ cm to $L^A_f = 0.69$ cm in length and layer B collapses from $L^B_0 = 4.34$ cm to $L^B_f = 1.60$ cm. Case A, at a final length of 2.27 cm, is the thinnest of all cases at the end of the simulation. Layer A in Case B ($L_{\text{tot}} = 5.44$) collapses from $L^A_0 = 2.2$ cm to $L^A_f = 1.52$ cm and Layer B collapses from $L^B_0 = 3.24$ cm to $L^B_f = 1.16$ cm. Layer A in Cases C ($L_{\text{tot}} = 5.24$) and D ($L_{\text{tot}} = 4.64$) does not collapse since the layer remains elastic and changes in front face positions observed in Fig. 14 are primarily due to rigid body motion. However, Layer B reduces from $L^B_0 = 4.04$ cm to $L^B_f = 1.54$ cm and $L^B_0 = 3.24$ cm to $L^B_f = 1.25$ cm for cases C and D respectively. The final system thicknesses of cases B, C, and D are 2.67 cm, 2.74 cm, and 2.65 cm respectively.

Fig. 15 shows the distal stresses for the one layer case and cases A through D. The overall behavior for the two layer cases is the same

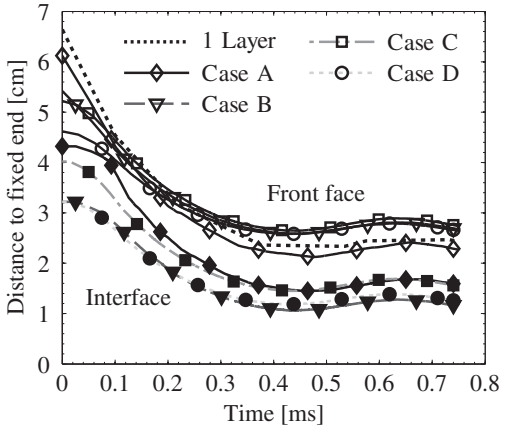

Fig. 14. Position of front face (empty markers) and material interface (filled markers) relative to the fixed end as a function of simulation time.

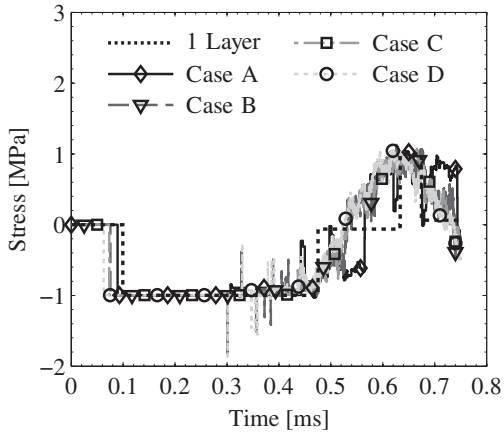

Fig. 15. Distal stress for optimum one and two layer cases.

despite the variability in layer lengths and densities. This behavior indicates that the second layer of material operates as a pulse modulator, taking an input from the first layer and transforming it into a desired profile on the fixed end. We note that this observation is in line with those made in [37] and [43], where it was reported that positioning the weakest material at the fixed end allowed for a lower transmitted load through the system. Compared to the one-layer case, Case *A* holds the compressive load for longer and has a longer duration tensile rebound from the fixed end. Cases *B*–*D* smooth out the transitions between compressive and tensile stresses. The pulse widths for the stresses beyond −1 MPa (between 0.3 ms and 0.4 ms) are very small (typically <0.1 μs) and satisfy the constraint over the impulse width.

In the optimal case for $\overline{\rho}_0^A = 0.06$, the whole two layer system undergoes densification. Although the minimum for $\overline{\rho}_0^A = 0.09$ does not completely densify (see Fig. 13), the first value of $\overline{\rho}_0^A = 0.09$ that satisfies the mass constraint ($L^A = 0.8$ cm, $L_{\text{tot}} = 5.84$ cm, $M = 0.376$ g, and indicated as the rightmost black diamond in Fig. 10(b)) is completely densified. Layer *A* in cases *C* and *D* is too stiff to undergo densification under the applied load. Therefore, absorptive capacity is not fully utilized. Layer *A*, in cases *C* and *D*, acts as a face sheet while layer *B* behaves as a core material. The stronger and heavier the face sheet, the less core is needed, and thus the shorter the system length. However, if mass is constrained, there is a diminishing return on increasing face sheet density.

5. Conclusions

The formation of shocks in two-layer cellular systems have been analyzed using the method of characteristics with thermodynamic shock theory. The EPD material model is proposed to capture the formation of shocks at the interface between material layers. We show that the RPPL model does not allow shock formation in two layer systems. The numerical implementation was verified against existing work. The two-layer analysis demonstrates that layer *A* is responsible for the majority of the energy dissipation when shocks form in both layers. The search for the optimum revealed that the higher the density of layer *A*, the shorter the total system length. However, there is a cost in mass associated with the reduction in total system length. The results further reinforce the established concept of sandwich materials, where a soft core is placed between stiff outer layers. Another finding in the optimization study is that, in all cases, the time for the material to dissipate the applied energy (minus remaining elastic energies) is the same at approximately $t = 0.42$ ms, meaning that a two layer configuration does not appear to improve dissipation rates.

The method as implemented is not restricted to two layers and could be executed for more interfaces. The primary drawback to this method is that it solves every wave reflection, and the number of wave reflections increases substantially for each material interface, resulting in large computational cost. Furthermore, the method as implemented only handles piece-wise constant loading inputs and additional work is required to handle problems that involve continuously varying loads.

References

[1] Gama BA, Bogetti TA, Fink BK, Yu CJ, Dennis Claar T, Eifert HH, et al. Aluminum foam integral armor: a new dimension in armor design. Composite Structures 2001;52(3–4):381–95. http://dx.doi.org/10.1016/S0263-8223(01)00029-0.

[2] Jang WY, Kyriakides S. On the crushing of aluminum open-cell foams: Part I. Experiments. International Journal of Solids and Structures 2009;46(34):617–34. http://dx.doi.org/10.1016/j.ijsolstr.2008.09.008.

[3] Mazor G, Ben-Dor G, Igra O, Sorek S. Shock wave interaction with cellular materials. Shock Waves 1994;3(3):159–65. http://dx.doi.org/10.1007/BF01414710.

[4] Elnasri I, Pattofatto S, Zhao H, Tsitsiris H, Hild F, Girard Y. Shock enhancement of cellular structures under impact loading: Part I experiments. Journal of the Mechanics and Physics of Solids 2007;55(12):2652–71. http://dx.doi.org/10.1016/j.jmps.2007.04.005.

[5] Deshpande VS, Fleck NA. High strain rate compressive behaviour of aluminium alloy foams. International Journal of Impact Engineering 2000;24(3):277–98.

[6] Edwin Raj R, Parameswaran V, Daniel B. Comparison of quasi-static and dynamic compression behavior of closed-cell aluminum foam. Materials Science and Engineering: A 2009;526(1–2):11–5. http://dx.doi.org/10.1016/j.msea.2009.07.017.

[7] Lopatnikov SL, Gama BA, Jahirul Haque M, Krauthauser C, Gillespie JW, Guden M, et al. Dynamics of metal foam deformation during taylor cylinder-hopkinson bar impact experiment. Composite Structures 2003;61(1–2):61–71. http://dx.doi.org/10.1016/S0263-8223(03)00039-4.

[8] Tan P, Reid S, Harrigan J, Zou Z, Li S. Dynamic compressive strength properties of aluminium foams. part I—experimental data and observations. Journal of the Mechanics and Physics of Solids 2005;53(10):2174–205. http://dx.doi.org/10.1016/j.jmps.2005.05.007.

[9] Guruprasad S, Mukherjee A. Layered sacrificial claddings under blast loading part I – analytical studies. International Journal of Impact Engineering 2000;24(9):957–73.

[10] Tan P, Reid S, Harrigan J, Zou Z, Li S. Dynamic compressive strength properties of aluminium foams. Part II–'shock' theory and comparison with experimental data and numerical models. Journal of the Mechanics and Physics of Solids 2005;53(10):2206–30. http://dx.doi.org/10.1016/j.jmps.2005.05.003.

[11] Langdon G, Karagiozova D, Theobald M, Nurick G, Lu G, Merrett R. Fracture of aluminium foam core sacrificial cladding subjected to air-blast loading. International Journal of Impact Engineering 2010;37(6):638–51. http://dx.doi.org/10.1016/j.ijimpeng.2009.07.006.

[12] Cui L, Kiernan S, Gilchrist MD. Designing the energy absorption capacity of functionally graded foam materials. Materials Science and Engineering: A 2009;507(1–2):215–25. http://dx.doi.org/10.1016/j.msea.2008.12.011.

[13] Hanssen AG, Enstock L, Langseth M. Close-range blast loading of aluminium foam panels. International Journal of Impact Engineering 2002;27(6):593–618. http://dx.doi.org/10.1016/S0734-743X(01)00155-5.

[14] Li QM, Meng H. Attenuation or enhancement—a one-dimensional analysis on shock transmission in the solid phase of a cellular material. International Journal of Impact Engineering 2002;27(10):1049–65. http://dx.doi.org/10.1016/S0734-743X(02)00016-7.

[15] Shim VPW, Tay BY, Stronge WJ. Dynamic crushing of strain-softening cellular structures—a one-dimensional analysis. Journal of Engineering Materials and Technology 1990;112(4):398–405. http://dx.doi.org/10.1115/1.2903349.

[16] Seitz MW, Skews BW. An analytical model for shock wave impact on compressible open-cell foam. Shock Waves 2007;16(4–5):287–98. http://dx.doi.org/10.1007/s00193-007-0073-2.

[17] Main JA, Gazonas GA. Uniaxial crushing of sandwich plates under air blast: Influence of mass distribution. International Journal of Solids and Structures 2008;45(7–8):2297–321. http://dx.doi.org/10.1016/j.ijsolstr.2007.11.019.

[18] Ashby MF, Evans A, Fleck NA, Gibson LJ, Hutchinson J, Wadley HN. Metal foams: a design guide. Boston: Butterworth Heinemann, ISBN 9780750672191; 2000. p. 40–54.

[19] Fleck NA, Deshpande VS. The resistance of clamped sandwich beams to shock loading. Journal of Applied Mechanics 2004;71(3):386–401. http://dx.doi.org/10.1115/1.1629109.

[20] Harrigan J, Reid S, Seyed Yaghoubi A. The correct analysis of shocks in a cellular material. International Journal of Impact Engineering 2010;37(8):918–27. http://dx.doi.org/10.1016/j.ijimpeng.2009.03.011.

[21] Ma G, Ye Z. Analysis of foam claddings for blast alleviation. International Journal of Impact Engineering 2007;34(1):60–70. http://dx.doi.org/10.1016/j.ijimpeng.2005.10.005.

[22] Li QM, Reid SR. About one-dimensional shock propagation in a cellular material. International Journal of Impact Engineering 2006;32(11):1898–906.
[23] Utku S. On the impact induced stress waves in long bars. Technical report 32–932. Pasadena, California: Califonia Institute of Technology, Jet Propulsion Laboratory; 1966. p. 21.
[24] Tran DVD, Singh MC. Nonlinear uniaxial thermoelastic waves by the method of characteristics. Journal of Thermal Stresses 2004;27(8):741–77. http://dx.doi.org/10.1080/01495730490440154.
[25] Kolsky H. Stress waves in solids. New York: Dover Publications; 1963. p. 208.
[26] Sumi N. Numerical solutions of thermoelastic wave problems by the method of characteristics. Journal of Thermal Stresses 2001;24(6):509–30. http://dx.doi.org/10.1080/01495730130015808 5.
[27] Lubliner J, Valathur M. Some wave-propagation problems in plastic–viscoplastic materials. International Journal of Solids and Structures 1969;5(12):1275–98. http://dx.doi.org/10.1016/0020-7683(69)90072-9.
[28] Maheo L, Viot P. Impact on multi-layered polypropylene foams. International Journal of Impact Engineering 2012. http://dx.doi.org/10.1016/j.ijimpeng.2012.03.011.
[29] Zeng H, Pattofatto S, Zhao H, Girard Y, Fascio V. Impact behaviour of hollow sphere agglomerates with density gradient. International Journal of Mechanical Sciences 2010;52(5):680–8. http://dx.doi.org/10.1016/j.ijmecsci.2009.11.012.
[30] Konstantinov GG, Marchenko LL, Shkhinek KN. Wave propagation in a finite elastoplastic bar with longitudinal impact. Combustion, Explosion, and Shock Waves 1967;1:39–42. http://dx.doi.org/10.1007/BF00748811.
[31] Guedes J, Rodrigues H, Bendse M. A material optimization model to approximate energy bounds for cellular materials under multiload conditions. Structural and Multidisciplinary Optimization 2003;25(5):446–52. http://dx.doi.org/10.1007/s00158-003-0305-8.
[32] Yu J, Li J, Hu S. Strain-rate effect and micro-structural optimization of cellular metals. Mechanics of Materials 2006;38(12):160–70. http://dx.doi.org/10.1016/j.mechmat.2005.05.018.
[33] Zhang W, Sun S. Scale-related topology optimization of cellular materials and structures. International Journal for Numerical Methods in Engineering 2006;68(9):993–1011. http://dx.doi.org/10.1002/nme.1743.
[34] Zhu F, Wang Z, Lu G, Zhao L. Analytical investigation and optimal design of sandwich panels subjected to shock loading. Materials & Design 2009;30(1):91–100. http://dx.doi.org/10.1016/j.matdes.2008.04.027.
[35] Shen C, Yu T, Lu G. Double shock mode in graded cellular rod under impact. International Journal of Solids and Structures 2013;50(1):217–33. http://dx.doi.org/10.1016/j.ijsolstr.2012.09.021.
[36] Ma GW, Ye ZQ. Energy absorption of double-layer foam cladding for blast alleviation. International Journal of Impact Engineering 2007;34(2):329–47.
[37] Pattofatto S, Elnasri I, Zhao H, Tsitsiris H, Hild F, Girard Y. Shock enhancement of cellular structures under impact loading: part II analysis. Journal of the Mechanics and Physics of Solids 2007;55(12):2672–86. http://dx.doi.org/10.1016/j.jmps.2007.04.004.
[38] Simo JC, Hughes TJR. Computational inelasticity. 1st ed. New York, NY: Springer, ISBN 9780387975207; 1998. p. 392.
[39] Gibson LJ, Ashby MF. Cellular solids: structure and properties. Cambridge, United Kingdom: Cambridge University Press, ISBN 9780521499118; 1999. p. 392.
[40] McCullough KYG, Fleck NA, Ashby MF. Uniaxial stress-strain behaviour of aluminium alloy foams. Acta Materialia 1999;47(8):2323–30. http://dx.doi.org/10.1016/S1359-6454(99)00128-7.
[41] Hanssen AG, Hopperstad OS, Langseth M, Ilstad H. Validation of constitutive models applicable to aluminium foams. International Journal of Mechanical Sciences 2002;44(2):359–406.
[42] Li QM, Mines RAW, Birch RS. The crush behaviour of rohacell-51WF structural foam. International Journal of Solids and Structures 2000;37(43):6321–41. http://dx.doi.org/10.1016/S0020-7683(99)00277-2.
[43] Occupant crash protection handbook for tactical ground vehicles. Warren, Michigan: United States Dept of the Army; 2000.
[44] Products & services. 2012. URL: http://www.rohacell.com.